Neuron, Volume *87*

Supplemental Information

Local Field Potentials Encode Place Cell Ensemble Activation during Hippocampal Sharp Wave Ripples

Jiannis Taxidis, Costas A. Anastassiou, Kamran Diba, and Christof Koch

SUPPLEMENTAL METHODS

LFP-sequences and firing rate-patterns

'LFP-sequences' over each ripple were computed by noting at each time point of the corresponding LFP-pattern the probe index with the highest z-scored ripple-amplitude. If at any point the maximum amplitude was the same in more than one probe, the one with the lowest index was chosen. 'Similarity' between pairs of sequences refers to either their average or their maximum correlation over lags within ±50 ms around the ripple peak (Figure S5).

'Firing rate-patterns' and 'sequences' where computed using the same analysis as for the corresponding LFP ones, with ripple-amplitudes replaced by the z-score normalized total firing rate from all spikes recorded by each probe. Firing rates were calculated over non-overlapping 4 ms-long bins. Similarity between firing rate-patterns or sequences is computed as before.

Self-Organized Mapping

Self-organized mapping (SOM) was used to classify LFP-patterns based on their overall spatiotemporal characteristics (Kohonen, 1995). Briefly, SOM classified a set of processed LFP-patterns onto a grid of map units through an unsupervised learning algorithm that preserves topological properties of the input. Thereby, after the training of the SOM grid, LFP-patterns with similar characteristics (in their processed version) were mapped onto neighborhoods of nearby units, with each LFP-pattern assigned to the map unit lying closest to it (in Euclidean distance). Subsequently, map units were segregated into clusters via K-means clustering in order to further group similar patterns that were mapped onto SOM unit neighborhoods.

Initially, to reduce the [probes x time bins] dimension of each LFP-pattern to few independent variables that can be used as input to the SOM algorithm, we performed two PCA analyses: (i) first, PCA was performed over all time points of each pattern, keeping only the first [probes-1] principal components and (ii) second, PCA was performed on this signal over all probes, keeping the first principal component. Thus, each pattern was represented in a reduced [probes-1]-dimensional space of principal components. After PCA, processed patterns were normalized to unit variance for efficient mapping and the SOM grid was set to 4x4 units for replay analysis, and 5x5 for all ripples in a session (to allow for a neighborhood of 1/[total grid size] for mapping each ripple type). Larger grid maps did not improve performance, as many units had no patterns mapped onto them. SOM was performed with linear initialization and long, batch training (Kohonen, 1995). Given the high variability in the pattern dataset and the preprocessing steps, assessment of SOM classification was based on partial preservation of topological characteristics in the average pattern mapped on each unit, as well as the fact that distinct neighborhoods of map units emerged with empty units between them.

Map units were then clustered through k-means clustering, setting three clusters for replay analysis. Setting two clusters did not alter our results whereas setting four clusters (one for each replay type) always left one 'empty' cluster containing units with no mapped patterns. Each LFP-pattern was assigned to the cluster of the unit that it was mapped on. The composition of each cluster (i.e. number of replays of each type over all ripples in the cluster) was tested against a random distribution by randomly redistributing all replays of a session onto the same clusters 1000 times. A cluster was set to contain significantly more replays of any given type than random, if their number had a percentile rank > 95% of the shuffled distribution (FDR-corrected for multiple comparisons in each session). We found no clusters that contained significantly more replays than the random distributions.

When analyzing all ripples in a session, SOM mapping revealed two distinct neighborhoods of units (Figure S7). K-means clustering segregated all SOM units into 2 clusters accordingly. Cluster 2 was set to be the cluster with the lowest average Euclidean distance of data points from the cluster centroid. In other words Cluster 2 was set to be the one containing more tightly clustered processed LFP-patterns. This definition is similar to the condition of highest average similarity between patterns used in Figure 7. On average, Cluster 2 had a larger size (mean fraction of ripples per cluster = 43.6% and 56.4%; $p < 0.001$, Wilcoxon test) and contained a larger fraction of replays (mean ratio of replays per cluster = 43% and 57%; $p < 0.001$, Wilcoxon test; only sessions with at least 4 replays included, $n = 30$). For illustration of SOM clustering, both processed patterns and SOM grid were projected onto the first two principal components space of the

patterns (Figure S7). The sequential-spiking content of each cluster was computed similarly as for similarity clustering (Figure 7).

Data normalization, SOM mapping, K-means clustering and analysis of SOM units, was performed using a publicly available Matlab toolbox (http://www.cis.hut.fi/somtoolbox/; developed by the Laboratory of Computer and Information Science, Helsinki University of Technology), along with custom written Matlab scripts.

SUPPLEMENTAL FIGURES

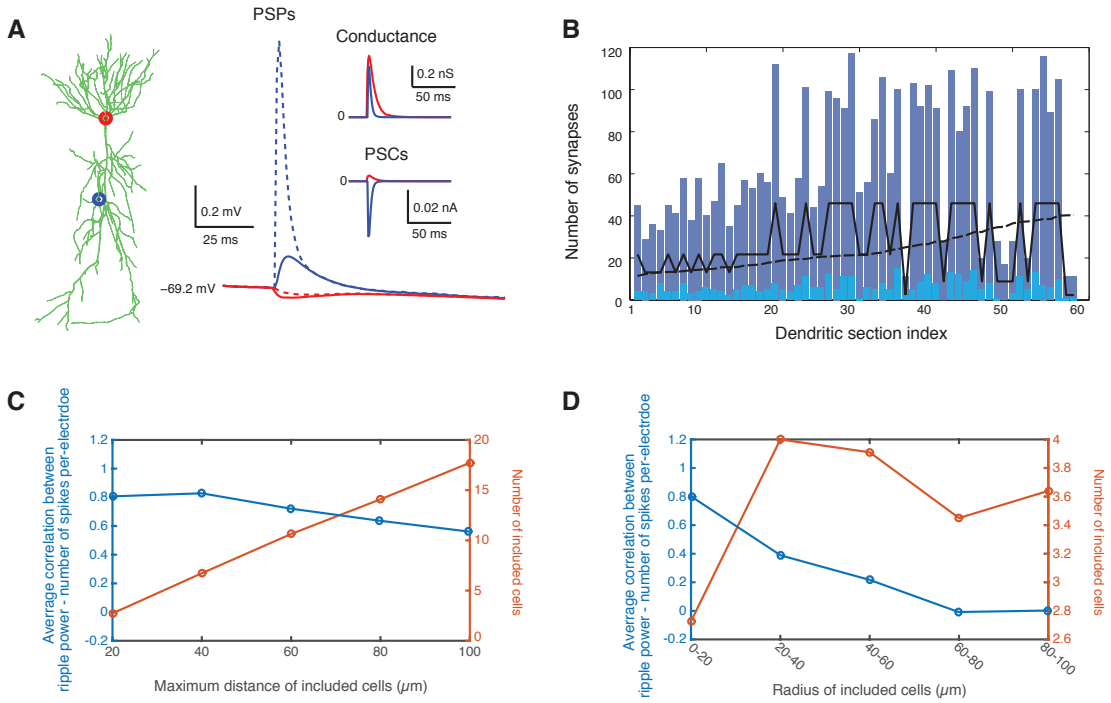

Figure S1: Related to Figures 1 and 2. Synaptic input in simulated pyramidal cells and dependence of ripple amplitude on distance of spiking cells. A: Left: Dendritic morphology of the multi-compartmental CA1 pyramidal neuron model. Two example synaptic locations are shown: One inhibitory synapse at the soma (red) and one excitatory synapse at an apical dendritic compartment within the stratum radiatum (blue). Right: PSPs from the activation of each of the two synapses at resting membrane potential (black line; ~ -69.15 mV). Dashed lines represent the membrane potential at the dendritic compartment and solid ones at the soma. Insets: Corresponding synaptic conductances (top) and postsynaptic currents at the two compartments. **B.** Distribution of excitatory synapses over the stratum radiatum dendritic sections of the strongly- and weakly-driven example cells (blue and cyan bars respectively) shown in Figure 1. Spine density (solid line) and section's distance from soma (dashed line) are also shown (a.u.). In both cells, the synaptic distribution follows the spine density distribution (Methods). **C.** Average correlation between ripple power and spike number, over 10 simulations, as a function of the distance of included cells from the electrode (blue). Correlations decrease when including spikes from distant cells, >40μm away from the electrode. The corresponding number of included cells is shown in red. **D.** Same when including cells within a given distance range. The number of included cells within each range remains relatively fixed but correlations decrease more rapidly than before and drop to zero for cells beyond ~60μm.

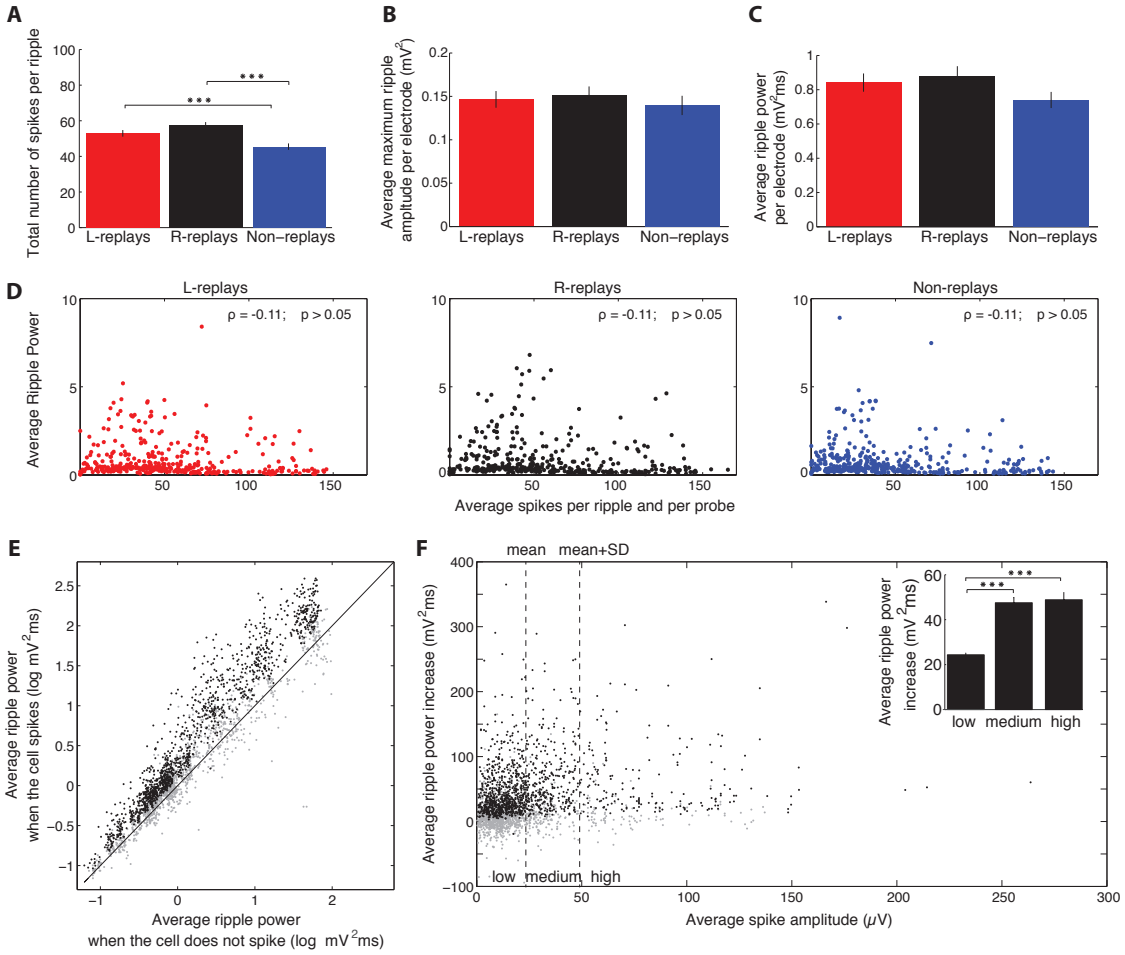

Figure S2: Related to Figure 4. Relationship between ripple power and spiking in recordings. A. Average number of spikes recorded during the three ripple categories (mean ± se; forward and reverse replays pooled). Replays were accompanied by a higher number of spikes ($p < 0.001$, Wilcoxon test). **B-C.** Average maximum ripple-amplitude (**B**) and ripple-power (**C**, total area under ripple-amplitude) at the average recording site, during the three ripple types. Differences were non-significant ($p > 0.05$, Wilcoxon test). **D.** From left: Average ripple power in each probe as a function of the average number of spikes recorded at the probe (interneuronal spikes omitted) during L-replays (left), R-replays (middle) and non-replays (right). No significant correlation was observed (in all cases: $\rho = -0.11$; $p > 0.05$, Student's t-test, FRD-corrected). **E.** Average ripple-power at the electrode where each cell was detected, when the cell spiked versus when it did not. Cells coinciding with significantly higher ripple-power when they spike, are shown in black (52%; $p < 0.05$, right-tailed Wilcoxon test; FDR-corrected) and the rest in grey. **F.** Percentage increase of average ripple-power when each cell spiked, relative to when it did not, as a function of the cell's average spike amplitude. There was no subset of large spike amplitude cells yielding high ripple amplitude increase. Dashed lines indicate mean spike amplitude (23.5 μV) and mean + SD (49 μV), used for splitting the cells into 'low', 'medium' and 'high spike amplitude' groups. Inset depicts the average ripple power increase in each group (mean ± se). 'Medium' and 'high' spike amplitude cells yield significantly higher ripple power increase compared to the 'low' group ($p < 0.001$; Wilcoxon test). Crucially, there is no statistically significant difference between 'high' and 'medium' groups. As such, the ripple amplitude is not formed by a few cells but, instead, is shaped by a large number of spiking neurons. (Black and grey cells correspond to the same groups as in **E)**.

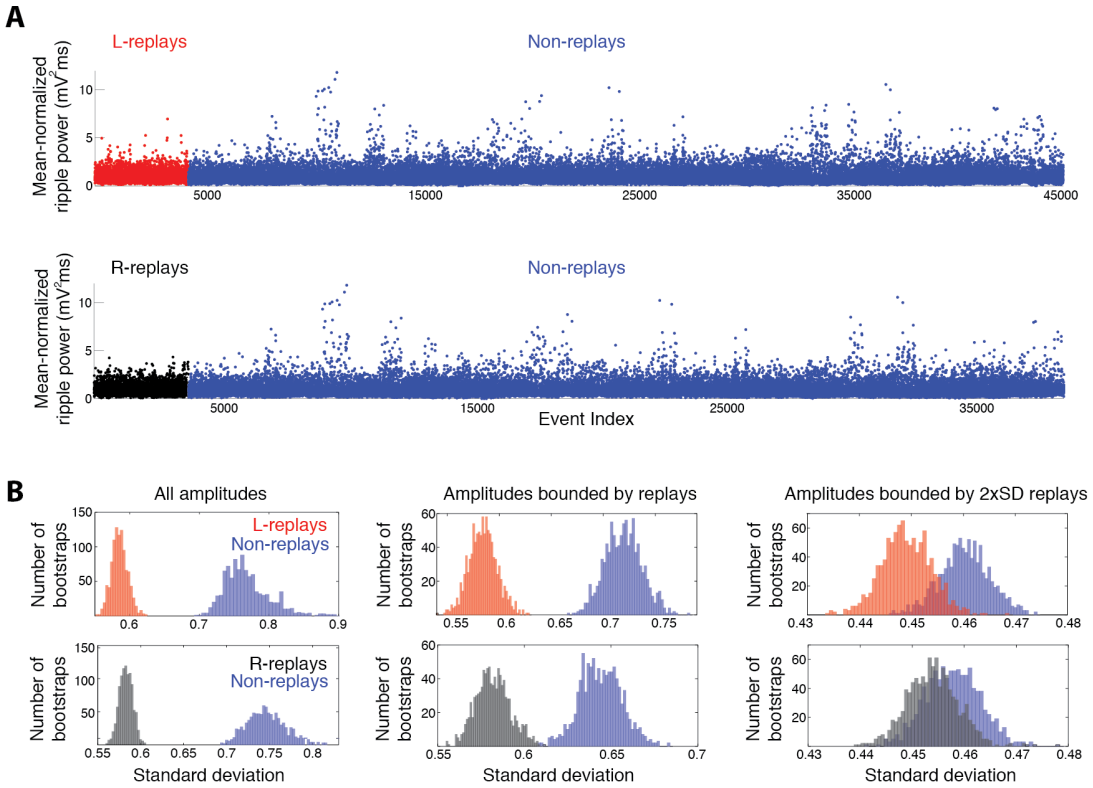

Figure S3: Related to Figure 5. A. Top: Ripple-power from all sessions and all probes containing L-sequence cells, during L-replays (red) and non-replays (blue). Power from each probe was mean-normalized for pooling. Bottom: Same for probes containing R-sequence cells and R-replays (black) versus non-replays (blue). **B.** Left: Distribution of ripple-power SD after bootstrapping (n = 1000 bootstraps) from the two corresponding populations. Middle: Same after removing any non-replays with absolute power beyond the maximum corresponding replay amplitudes (see text). Right: Same after further removing any events lying beyond mean ± 2SD of the corresponding replay set. In all cases, mean SD was significantly lower for replays than non-replays ($p < 0.001$, Wilcoxon test).

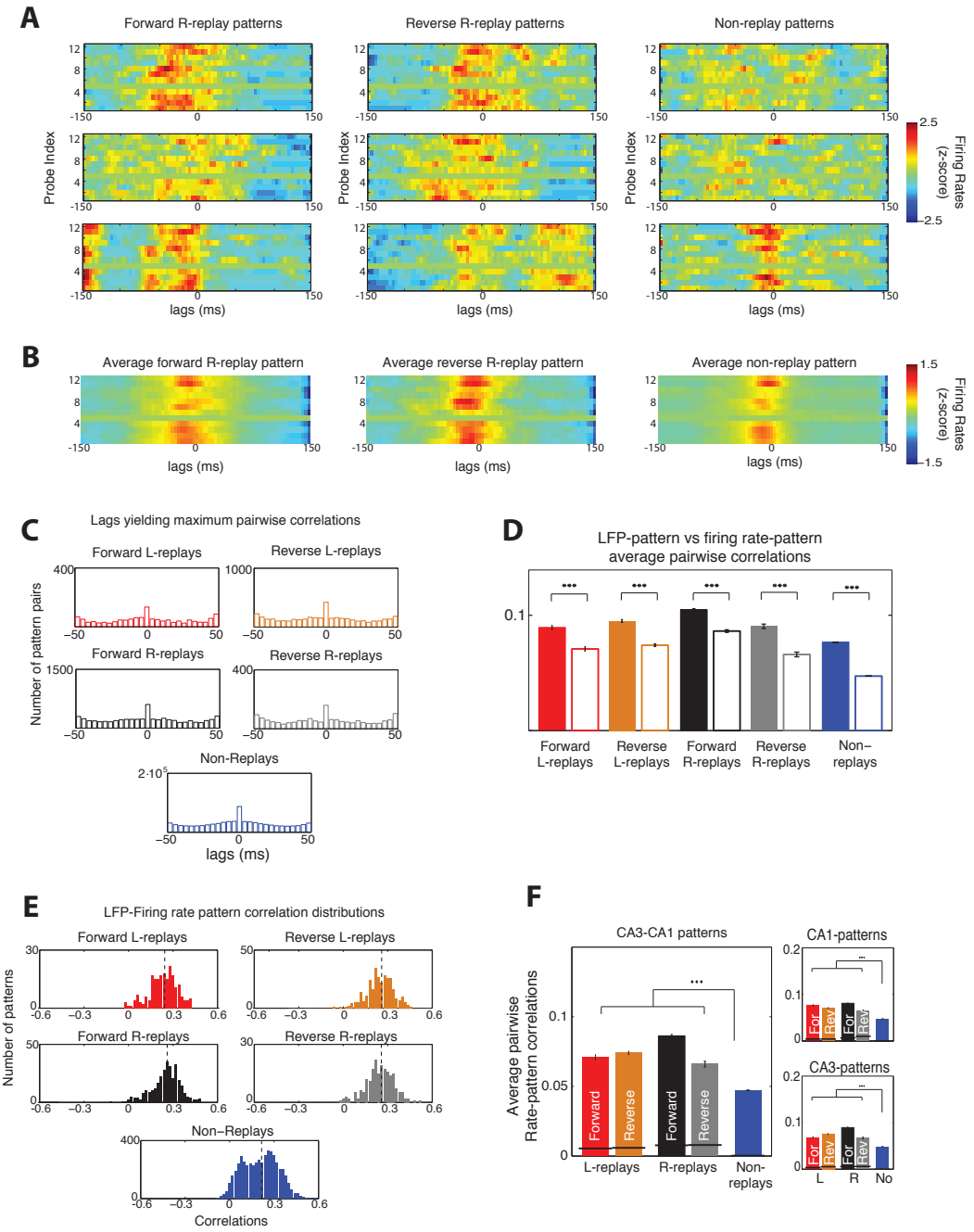

Figure S4: Related to Figure 6. Firing-rate patterns of ripple events. A. Example firing-rate patterns from the same ripple events as in Figure 6A. **B.** Average patterns from the corresponding ripple types in the example session. **C.** Distribution of lags yielding maximum-correlations for all ripple types. Unlike LFP-patterns, distributions are close to uniform. **D.** Average pairwise similarity between LFP-patterns (filled bars) was significantly higher than that between firing rate-patterns (empty bars) for all ripple types ($p < 0.001$, Wilcoxon test, FDR-corrected). **E.** Distributions of correlation between the LFP-pattern and the firing rate-pattern of each ripple. Correlations were significantly positive ($p < 0.05$, sign test, FDR-corrected) suggesting a partial overlap of the two pattern types. **F.** Average pairwise similarity (mean ± se) between firing rate-patterns for all replay types were significantly higher than those for non-replays (asterisks; $p < 0.001$, Wilcoxon test, FDR-corrected). Black lines indicate chance-similarity baselines. Right: Same for patterns computed only over the CA1 (top) and CA3 probes (bottom).

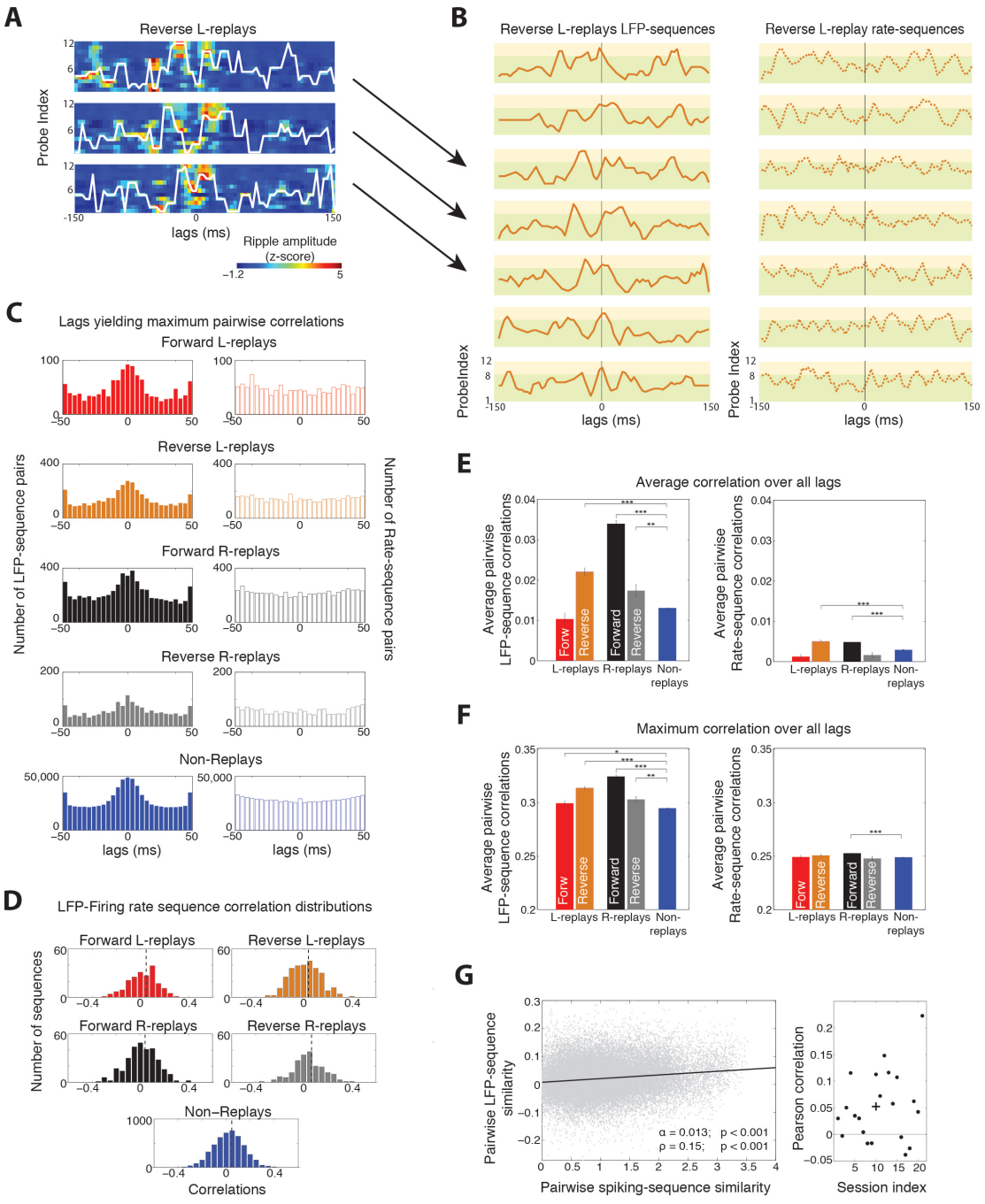

Figure S5. Related to Figure 6. Replays of place cell sequences yield more consistent 'LFP-sequences' than non-replays. A. Examples of LFP-patterns during three reverse L-replays from one recording session. 'LFP-sequences' (white traces) illustrate the probe index with the maximum z-scored ripple amplitude at each time point of the ripple. Probes 1-8 and 9-12 are located in the CA3 and CA1 pyramidal layers respectively. **B.** Left: LFP-sequences from eight consecutive reverse L-replays (smoothed for plotting clarity). Arrows indicate the three examples in A (differences due to smoothing). Green and yellow background indicates CA3- and CA1-located probes respectively. Black lines point the CA1 ripple-peak (0 ms). Right: Firing rate-sequences of the same replays, calculated using the firing rate-pattern of each event instead of its LFP-pattern. **C.** Distributions of lags yielding maximum pair-wise correlations between LFP-sequence pairs (left) and rate-sequence pairs (right; n = 21 sessions pooled). Unlike LFP-

sequences, distributions of Rate-sequence lags are close to uniform. **D.** Distributions of correlations between the LFP-sequence and the rate-sequence or each event in all ripple types. Correlations were significantly positive ($p < 0.001$, sign test, FDR-corrected). **E-F**. Left: Average pairwise correlations (mean ± se) between sequences for all replay types and non-replays (averaged over all sessions; all sessions pooled). Right: Same for firing rate-sequences. Correlations stand either for the average correlation (**E**) or the maximum correlation over all accounted lags (**F**). All replay types have significantly more similar LFP-sequences than non-replays using either measure (with the only exception of forward L-sequences when using lag-averaged correlations). Rate-sequences of most replay-types did not exhibit such pronounced effects. **G.** The spiking similarity between ripple pairs was significantly correlated with their LFP-sequence similarity (same example session as in Figure 6K; line: least squares linear fit; α: slope, $p < 0.001$, F-test; ρ: Pearson correlation, $p < 0.001$, Student's t-test). Right: Distribution of Pearson correlations computed for each session. The average per-session correlation ($<\rho> = 0.052$; cross) was again significantly positive ($p < 0.05$; right-tailed sign test). Asterisks: one, $p < 0.05$; two, $p < 0.01$; three, $p < 0.001$, Wilcoxon test, FDR-corrected).

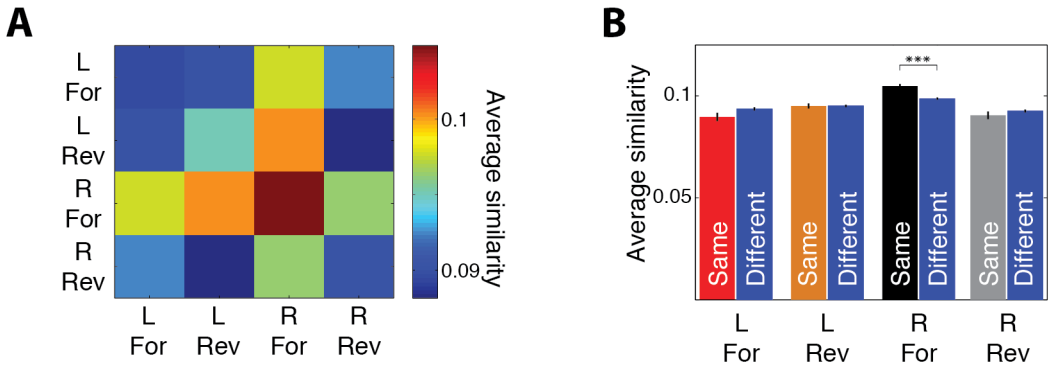

Figure S6: Related to Figure 6. Similarity analyses of LFP-patterns during replays. A. Average similarity between all combinations of replay types. **B**. Average similarity (mean ± se) between replays of a given type (color) and between replays of that type and all others (blue). Except for forward R-replays, no other type exhibits higher within-group similarity than between groups. Asterisks: $p < 0.001$; Wilcoxon test; FDR-corrected.

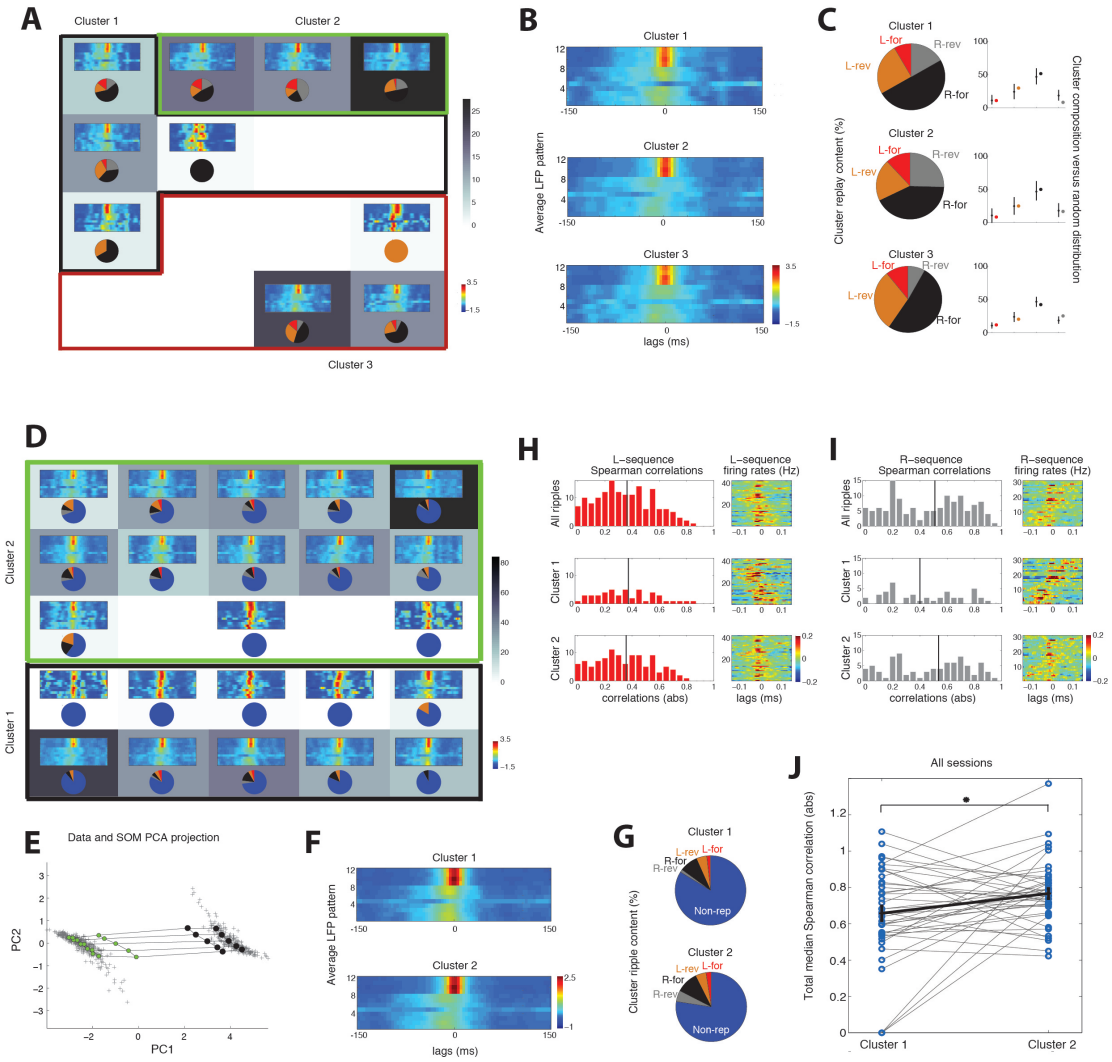

Figure S7: Related to Figure 7. Classifying LFP-patterns through self-organized mapping (SOM) and clustering the map units segregates ripples with replay content from non-replays, but not different replay-types. A. Replay LFP-patterns from one example recording session, classified into SOM units. Each cell represents one unit, color coded by the number of patterns mapped to the unit. Empty cells reflect units without any patterns mapped onto them. The average pattern and the replay composition of all patterns in each unit are also shown (color indexes are same as in **B**). Units were grouped into 3 clusters, using K-means clustering. **B.** Average LFP-pattern in each cluster. **C.** (Left) Composition of each cluster. Different replay-types are shown in different color. (Right) Ratio of each replay-type in each cluster compared to a random distribution of replays into a cluster of the same size (mean ± 95% confidence intervals). Replays were not efficiently segregated into different replay types. **D.** Same as in **A** for a SOM of all ripples from the same recording session (also same session as in Figure 7). Units were split into two clusters with Cluster 2 being the one with more tightly clustered patterns. **E.** SOM map grid (circles) displaying the two clusters (green and black) and the original processed patterns (crosses), projected onto the first two principal components of the dataset. **F-G.** Same as **B-C** for the SOM over all ripples. Cluster 2 contained a higher percentage of replays than Cluster 1. **H.** Left: Histogram of Spearman correlations (absolute values) of the L-sequence over all ripples (top), ripples contained in Cluster 1 (middle) and Cluster 2 (bottom). Vertical lines indicate medians. Right: Average z-scored firing rates of L-sequence over the corresponding sets of ripples. Cells are stacked according to their place field. **I.** Same as G for the R-sequence. Cluster 2 contains ripples with higher sequential spiking content. **J.** Distribution of total median Spearman correlations over ripples in the two clusters for all recording sessions (blue points). Black line depicts average over all sessions (mean ± se). Cluster 2 contains, on average, ripples with more correlated sequential spiking ($p < 0.05$; 2-sample t-test).